Mon. Not. R. Astron. Soc. **000**, 1–16 () Printed 11 February 2005 (MN LATEX style file v2.2)

Very Small Array observations of the Sunyaev–Zel'dovich effect in nearby galaxy clusters

Katy Lancaster[1,7], Ricardo Genova-Santos[2], Nelson Falcòn[2,6], Keith Grainge[1], Carlos Gutièrrez[2], Rüdiger Kneissl[1], Phil Marshall[4], Guy Pooley[1], Rafael Rebolo[2,5], Jose-Alberto Rubiño-Martin[2], Richard D. E. Saunders[1], Elizabeth Waldram[1], Robert A. Watson [3].

[1] *Astrophysics Group, Cavendish Laboratory, University of Cambridge, Madingley Road, Cambridge CB3 0HE*
[2] *Instituto de Astrofisíca de Canarias, 38200 La Laguna, Tenerife, Canary Islands, Spain*
[3] *Jodrell Bank Observatory, University of Manchester, Macclesfield, Cheshire SK11 9DL*
[4] *Kavli Institute for Particle Astrophysics and Cosmology, Stanford University PO Box 20450, MS29, Stanford, CA 94309, USA*
[5] *Consejo Superior de Investigaciones Cientificas, Spain*
[6] *Dpt. de Fisica, FACYT, Universidad de Carabobo, Venezuela*
[7] *Present address: Physics Department, University of Bristol, Tyndall Avenue, Bristol BS8 1TL*

Received **insert**; Accepted **insert**

ABSTRACT

We present Very Small Array (VSA) observations (centred on $\approx 34\,\mathrm{GHz}$) on scales $\approx$ 20 arcmin towards a complete, X-ray–flux–limited sample of seven clusters at redshift $z < 0.1$. Four of the clusters have significant Sunyaev-Zel'dovich (SZ) detections in the presence of CMB primordial anisotropy. For all seven, we use a Bayesian Markov-Chain-Monte-Carlo (MCMC) method for inference from the VSA data, with X-ray priors on cluster positions and temperatures, and radio priors on sources. In this context, the CMB primordial fluctuations are an additional source of Gaussian noise, and are included in the model as a non–diagonal covariance matrix derived from the known angular power spectrum. In addition, we make assumptions of β–model gas distributions and of hydrostatic equilibrium, to evaluate probability densities for the gas mass ($M_{\rm gas}$) and total mass ($M_{\rm r}$) out to r_{200}, the radius at which the average density enclosed is 200 times the critical density at the redshift of the cluster. This is further than has been done before and close to the classical value for a collapsed cluster. Our combined estimate of the gas fraction ($f_{\rm gas} = M_{\rm gas}/M_{\rm r}$) is $0.08^{+0.06}_{-0.04}h^{-1}$. The random errors are poor (note however that the errors are higher than would have been obtained with the usual chi-squared method on the same data) but the control of bias is good. We have described the MCMC analysis method specifically in terms of SZ but hope the description will be of more general use. We find that the effects of primordial CMB contamination tend to be similar in the estimates of both $M_{\rm gas}$ and $M_{\rm r}$ over the narrow range of angular scales we are dealing with, so that there is little effect of primordials on $f_{\rm gas}$ determination. Using our $M_{\rm r}$ estimates we find a normalisation of the mass – temperature relation based on the profiles from the VSA cluster pressure maps that is in good agreement with recent $M - T$ determinations from X-ray cluster measurements.

Key words: cosmology: observations – cosmic microwave background – galaxies: clusters: individual (Coma, A1795, A399, A401, A478, A2142, A2244) – X-rays:galaxies:clusters

1 INTRODUCTION

Galaxy clusters have long been thought to provide a faithful sample of cosmic baryonic matter (see e.g. White et al. (1993), Evrard (1997)). One quantity often calculated and assessed in such work is the gas fraction $f_{\rm gas}$, which is defined as the (baryonic) gas mass over the total (baryonic plus dark matter) mass of the cluster. We here present Sunyaev Zel'dovich (SZ) (Sunyaev & Zel'dovich (1972), see also e.g. Birkinshaw (1999), Carlstrom et al. (2002)) observations of

a sample of clusters, from which we infer $f_{\rm gas}$. Our random errors are high but the sample is complete, the redshifts deliberately low, and we are able to estimate $f_{\rm gas}$ out to radii at which the overdensity of the enclosed region is close to the classical value of 178 for a collapsed object (see e.g. Peacock (1999)). First we review some of the existing $f_{\rm gas}$ measurements.

A popular route in investigating cosmic baryonic matter is the detailed study of the X-ray emission from cluster gas. For example, in an investigation based on *ROSAT* PSPC data (Ettori & Fabian (1999)), a sample of 36 clusters of redshift $0.05 \leqslant z \leqslant 0.44$ was used to measure $f_{\rm gas}$. Assumptions of isothermality and hydrostatic equilibrium were required. The resulting $f_{\rm gas}$ distribution (within r_{500}, that is, where the mean density inside this radius is 500 times the critical density at the redshifts of the clusters) was centred on a value $f_{\rm gas}(r_{500}) = 0.168 h_{50}^{-1.5}$. Values for individual clusters were found to vary between 0.101 and 0.245. Mohr et al. (1999) also analysed PSPC data on 45 X-ray selected clusters, finding a mean $f_{\rm gas}(r_{500})$ of $0.212 h_{50}^{-1.5}$ in a subsample of 27 clusters hotter than 5 keV. Allen et al. (2002), following a similar route (supplemented by gravitational lensing information on the total mass) with *Chandra* imaging spectrometer data find, for a set of six clusters with $0.103 \leqslant z \leqslant 0.461$, a mean $f_{\rm gas}$ within r_{2500} of $0.113 \pm 0.005 h_{70}^{-1.5}$ for a Λ–CDM model, a very precise determination with very similar values for each cluster. Allen et al. (2003), with additional data, investigated the observed change of $f_{\rm gas}$ with cosmology.

Studies making use of the SZ effect have potential advantages for gas and gravitational potential measurements (where the potential is obtained via calculation of the total mass). The X-ray signal is proportional to $n_{\rm e}^2$ (where $n_{\rm e}$ is electron density), while the SZ signal is proportional to $n_{\rm e}$. This means that SZ is less biased to concentration and can constrain clumping. Although X-ray telescopes achieve excellent signal to noise, they are restricted to observing the denser, inner regions of a cluster (e.g out to r_{2500}). With SZ it is possible to measure $n_{\rm e}(r)$ over a larger range of r (e.g. close to the virial radius) as less dynamic range is required.

Myers et al. (1997) used the OVRO 5.5m telescope to observe the SZ effect in 3 clusters at 32 GHz. With the addition of the Coma cluster (observed by Herbig et al. (1995)), they obtain a gas fraction of $f_{\rm gas} = 0.061 \pm 0.011 h_{100}^{-1}$ This sample of objects lies in the redshift range $0.023 \leqslant z \leqslant 0.0899$, and includes three clusters which we also present here. (Mason et al. (2001) extend the sample to seven clusters, incorporating a further two discussed in this paper. The data were used to calculate H_0.)

Grego et al. (2001) used the OVRO and BIMA arrays to make SZ observations of galaxy clusters at 30 GHz. The data were used to infer the gas mass and total mass, thus constraining $f_{\rm g}$ (within r_{500}) in 18 X-ray selected clusters in the redshift range $0.171 \leqslant z \leqslant 0.826$. The mean value obtained for the full sample was $f_{\rm gas} = 0.081^{+0.009}_{-0.011} h_{100}^{-1}$. In addition, a 'fair' subsample is defined as the five most X-ray luminous clusters in the EMSS sample. These objects have redshift $0.328 \leqslant z \leqslant 0.826$, and together give a mean gas fraction $f_{\rm gas} = 0.089^{+0.018}_{-0.019} h_{100}^{-1}$.

One of the aims of the VSA project (Watson et al. (2003), Taylor et al. (2003), Scott et al. (2003), Rubiño-Martin et al. (2003), Grainge et al. (2003), Slosar et al. (2003) Dickinson et al. (2004), Rebolo et al. (2004)) has been to image nearby, massive clusters in SZ. The VSA baselines at ≈ 34 GHz couple well to the angular scales of such clusters. Here we describe SZ observations and cluster–parameter inferences of an X-ray selected, complete sample of seven clusters, with redshift $0.023 \leqslant z \leqslant 0.098$ and median 0.075. The age of the Universe at z = 0.075 is 1.7 times its age at $z = 0.55$. The importance of low–z work is illustrated by the following two points:

- The low redshifts of the clusters mean that they have particularly good X-ray data, and one can be reasonably confident that bright X-ray selected complete samples are in fact complete.
- Since clusters grow under gravity, then on average low redshift clusters should be more evolved than those at higher redshift. Comparison of, for example, $f_{\rm gas}$ in low- and high-z samples is important. (Of course, we do not know how big the samples have to be to encompass meaningful averages).

One immediate difficulty on these angular scales is contamination by CMB primordial anisotropy. At the start of this VSA observational programme, it was evident that we needed an analysis method that would apply the inference process correctly and would properly cope with error distributions in low signal–to–noise situations. There is the additional difficulty of dealing with (potentially variable) radio sources at 34 GHz. This could be especially problematic where sources are in the clusters themselves rather than in the background: the low redshifts of the clusters imply such sources may be very bright. Accounting for these effects correctly necessitates the exploration of the posterior probabilities of the parameters of a β–model for the gas distribution given the VSA visibilities, receiver noise, the CMB and radio sources. The method must also incorporate prior knowledge on e.g. the cluster positions from X-rays, and on source fluxes in a way which can cope with variability. We assume isothermality, and that the clusters are well described by hydrostatic equilibrium. We use a Markov Chain Monte Carlo (MCMC) sampler (`BayeSys`) for an acceptable combination of speed and accuracy.

In section 2 we briefly describe the relevant features of the VSA. In section 3 we present the sample, outline the data reduction pipeline and describe our strategy for dealing with radio sources. In section 4 we present our results, and attempt to describe the Bayesian analysis method in non-specialist terms. We make concluding comments in section 5.

2 THE VERY SMALL ARRAY

The VSA is a 14–element interferometric telescope situated at the Observatorio del Teide, Tenerife. The observing frequency is tunable in the 26–36 GHz range, with a bandwidth of 1.5 GHz; at these frequencies observations should be relatively free from contamination by Galactic foregrounds for fields at high Galactic latitude. The 14 antennas are identical. They rotate independently and are mounted on a tilting table thus allowing tracking in two dimensions. The table is surrounded by an aluminium shield to prevent groundspill.

The telescope was designed to operate in two configurations: Compact (see e.g. Watson et al. (2003) for tech-

nical details) and Extended (see Grainge et al. (2003)). All data in this paper were taken using the extended configuration. The Extended Array has 322–mm diameter illuminated apertures, resulting in a primary beam of 2.0° FWHM when operating at 34 GHz. The horn arrangement on the table allows for a range of baselines between approximately 40 cm and 3 m. The telescope is sensitive to angular sizes in the range $0.25^\circ < \theta < 1.2^\circ$, and is ideal for observing low redshift clusters.

Radio sources are a problem in all cm–wave CMB observations at all but the lowest angular resolutions, and SZ is no exception. The VSA design includes a dedicated source–subtraction telescope. This comprises two 3.7 m dishes located next to the main array and used as an interferometer with a 9 m baseline, giving 4 arcmin resolution and a 9 arcmin field of view. The source–subtractor does not resolve any of the sources which we observe, but resolves out the CMB fluctuations.

3 OBSERVATIONS

3.1 Galaxy Clusters

The VSA targets were selected from the Northern ROSAT All-Sky Survey (Böhringer et al. (2000), NORAS hereafter) as the seven most X-ray luminous objects at redshift < 0.1. The clusters have rest–frame X-ray luminosity $> 5 \times 10^{37}$ W in the 0.1–2.4 keV energy band. Additionally, only clusters observable from Tenerife and Cambridge were considered. This imposed declination limits of $10^\circ < \delta < 60^\circ$. The upper limit is set by the latitude and configuration of the VSA main array. The lower limit is set by the need for the use of the Ryle Telescope (RT) as part of the source–subtraction strategy (see section 3.3). Note that we have *not* applied any criteria concerning fluxes of contaminant radio sources. This is unlike the VSA primordial work, and indeed the SZ work of the RT and OVRO/BIMA.

Pointing centres for the seven fields were defined based on the X-ray positions of the clusters as published in NORAS. Data for each target were obtained in a series of short observations made during the period October 2001–August 2003. Repeat observations were required in several cases due to uncharacteristically persistent bad weather. The sample is summarised in Table 1, along with published redshifts, temperatures used in our analysis, X-ray luminosities and total integration times of the VSA observations. The clusters A401 and A399 are only separated by around a degree, so were observed in a single pointing centred on A401.

3.2 Calibration and Data Reduction

The primary calibrator for all VSA observations is Jupiter. We based our calibration scale on the effective temperature of the planet at 34 GHz: $T_{34} = 155 \pm 5$ K (Mason et al. (1999)). The flux scale is transferred to our other calibration sources: Cas A and Tau A. The calibrators are observed on a daily basis, allowing flux and phase calibration at regular intervals. Cas A and Tau A are partially resolved on the longest VSA observations: we overcome this problem by applying models as discussed in Grainge et al. (2003). Full details of the VSA calibration will be presented in a forthcoming paper. Note that in Dickinson et al. (2004) and Rebolo et al. (2004) we re-scale our calibration to agree with the recent WMAP results.

The data reduction pipeline for galaxy clusters is identical to that employed in the processing of our CMB data, and is presented in detail in Watson et al. (2003). Each observation is analysed independently using the `reduce` software, developed by the VSA team. The procedure is now highly developed, allowing virtually automatic correcting, flagging, filtering and re-weighting of the data. However, each raw data file must be checked by eye at least once to eliminate some 'bad' data (due to bad weather or telescope malfunction), and to ensure optimum quality in the reduced data. It is also necessary to identify files requiring special filtering depending on where the Sun, Moon or a bright planet was during the observation. The resulting calibrated visibilities from each observation are taken and stacked together.

The data were reduced independently by the groups at the Cavendish, the IAC and JBO, and the results found to be fully consistent. Approximately 28% of the data were discarded due to bad weather, filtering and telescope down–time.

The form of data from the single baseline source–subtraction interferometer is identical to that of the main array and is processed in a similar way. The primary flux calibrator is NGC 7027. The flux scale from this is applied to our other flux calibrators. We use interleaved calibrators in order to monitor the telescope phase.

3.3 Radio Sources

Contamination by radio sources can be a large problem for CMB observations. The contribution goes as ℓ^2 so tends to be more problematic for the (often higher-resolution) SZ work than for primordial CMB observations. In order to map the SZ effect accurately, it is necessary to account for the effect of radio sources which may be part of, in front of, or behind the cluster. The VSA source–subtraction interferometer allows potentially problematic sources to be observed simultaneously with main array observations of the cluster fields.

As no high frequency ($\approx$34 GHz) survey of the radio sky is available, we scheduled source observations via a two–fold approach:

- The NVSS and GB6 catalogues (Condon et al. (1998), Gregory et al. (1996)) were examined for sources within a radius of 2° from the cluster centres. Source fluxes at 1.4 and 4.9 GHz were used to perform a simple extrapolation to 30 GHz, thus making some prediction of the approximate level of contamination in the SZ observations. All sources with predicted flux greater than 50 mJy were selected for observation with the VSA source–subtractor.
- In order to account for flat or rising spectrum sources not seen at the lower frequencies, the RT was used to survey the central square degree of each field at 15 GHz with the rastering technique described by Waldram et al. (2003). Peaks $\gtrsim$20 mJy in the raster maps were recorded and the corresponding position list was added to the source subtractor observing queue. This ensured that we accounted not only for all potentially bright sources in the field, but also

Table 1. The VSA cluster sample: Cluster coordinates (Böhringer et al. (2000)), redshift (Struble & Rood (1991)), electron temperature (Markevitch et al. (1998)), except Coma, Hughes et al. (1988), X-ray luminosity (Böhringer et al. (2000)), integration time, map rms (outside the primary beam).

Cluster	RA (B1950)	Dec (B1950)	z	T_e (keV)	L_X (10^{37}W)	$T_{\rm int}$ (Hours)	rms (Jy)
Coma	12 57 18.29	28 12 28.5	0.0232	9.1 ± 0.7	7.01	80	0.021
A1795	13 46 34.43	26 50 37.5	0.0616	7.8 ± 1.0	9.93	115	0.020
A399	02 55 05.33	12 50 57.6	0.0715	7.0 ± 0.4	6.78	96	0.030
A401	02 56 12.55	13 22 50.1	0.0748	8.0 ± 0.4	11.76	96	(As A399)
A478	04 10 40.89	10 20 26.0	0.0882	$8.4^{+0.8}_{-1.4}$	13.31	74	0.018
A2142	15 56 16.45	27 22 08.0	0.0899	$9.7^{+1.5}_{-1.1}$	20.52	73	0.023
A2244	17 00 52.86	34 07 54.5	0.0980	$7.1^{+5.0}_{-2.2}$	7.39	91	0.018

for fainter sources which may have been present in the critical central regions of the SZ fields.

A summary of the source lists for all clusters is presented in Table 2, including fluxes measured by the source–subtractor. The 15 GHz fluxes are those from RT pointed observations. Whereas for our primordial anisotropy work source fluxes were subtracted directly from the visibilities, we choose here to use our measured fluxes as priors in the Bayesian fitting software. Due to telescope malfunction at various stages during our observing schedule, not all sources were observed simultaneously with the corresponding cluster. In order to account for possible variability in the source flux, broader priors were used than would have been assumed otherwise. Directly subtracting source fluxes with such uncertainties would lead to biases when fitting to the SZ data.

We can assess how much the SZ detections are affected by confusion noise from sources not found in the above, as follows. A corollary of Scheuer's work (Scheuer (1957)) is that confusion is worst when there is ≈ 1 source per synthesised beam. Examination of Table 2 shows that in the RT surveying, at about 20 mJy there is less that one source per VSA average SZ synthesised beam. A rough extrapolation indicates that there is one source per beam at 34 GHz at a level of 10 mJy. Since the detected SZ fluxes are ≈ 150 mJy, it is evident that the source strategy is adequate.

4 RESULTS

4.1 Maps

The flagged and stacked data are held as visibility files, containing the real and imaginary part for each observed uv–position along with an associated rms noise level. Standard AIPS tasks are used to make maps, and to perform CLEANing using one CLEAN box encompassing the area of the VSA primary beam. All analysis and parameter fitting is performed in the visibility plane; the maps presented here along with the resulting discussion are included purely to illustrate the results of our SZ programme.

We expect a larger SZ response on the shortest baselines, so an appropriate Gaussian taper is applied in each case. This emphasises structure on large scales. Taper values were chosen based on the range of uv radii available in each cluster's data. In order to determine appropriate tapers for our sample, we used cluster parameters from Mason et al. (2001) (as listed in Table 5) to generate predicted SZ profiles. These are shown in Figure 1. (We observe that the Mason et al. (2001) value for the core radius of A399 (4.33 ± 0.45 arcmin) is in direct conflict with that reported by Sanderson & Ponman (2003) (1.89 ± 0.36 arcmin). The use of Mason et al.'s parameter may result in an over-estimate of the SZ flux from this cluster.) The chosen tapers are ≈ 0.1kλ, although the taper for Coma would ideally be ≈ 0.023kλ. This cuts out nearly all Extended Array baselines, so a value of ≈ 0.1kλ was used with good results. These maps of the VSA cluster sample are presented in Figure 2. The contours are 1.5σ, where σ is the rms noise level presented in Table 1. We comment on the significance of the detections in each map, and also the strength of the observed primordial features. We emphasise that this is not intended to be a quantitative analysis of the signal to noise ratio achieved for each cluster.

4.1.1 Coma: Map (a)

Coma is at redshift $z = 0.0232$, giving it an angular size on the sky roughly four times greater than any other cluster in the sample. It would ideally be observed on baselines even shorter than those of the VSA. However, the SZ signal from this cluster is so strong, we detect it at 7.5σ. 4.5σ primordial features are visible around the SZ decrement.

4.1.2 A1795: Map (b)

A1795 is also detected at the 7.5σ level. This map contains a bright positive primordial feature south of the cluster.

4.1.3 A399 and A401: Map (c)

A399 does not appear in the map. We argue that this is most probably due to contamination by primordial CMB. Although the contours are negative at the position of A401, we suggest that this is largely due to the primordial decrement east of the cluster position. The SZ signal from the cluster may be contributing in part, but it is important not to confuse the two effects. The centre of the obvious decrement is around 15 arcmin away from the X-ray centre of A401.

4.1.4 A478: Map (d)

The A478 map shows a 6σ SZ detection. Primordial CMB structures are visible all around the cluster, varying in strength from 3–4.5σ.

Table 2. Radio sources present in the cluster fields. The asterisked source was predicted to have flux less than 50 mJy, but Mason et al. (2001) suggest it may be variable.

	RA	Dec	Predicted Flux 34 GHz	RT Survey 15 GHz	VSA Source–Subtractor 34 GHz
	(B1950)	(B1950)	(mJy)	(mJy)	(mJy)
Coma	12 48 36	+28 39 47	75		46 ± 11
	12 49 25	+28 07 55	71		29 ± 9
	12 50 49	+27 55 57	99		82 ± 8
	12 51 46	+27 53 41	311		250 ± 3
	12 54 04	+27 17 17	57		56 ± 5
	12 55 36	+28 36 36	96	49 ± 3	26 ± 9
	12 56 08	+29 25 19	53		10 ± 12
	12 57 11	+28 13 40	-	27 ± 3	34 ± 7
	12 58 04	+28 46 18	226	251 ± 13	207 ± 10
	12 58 56	+28 37 45	-	34 ± 3	31 ± 5
	12 58 59	+28 58 59	168		10 ± 7
	12 59 58	+27 25 17	58		49 ± 9
	13 03 59	+27 18 37	52		45 ± 9
A1795	13 39 50	+27 24 42	521		380 ± 9
	13 45 45	+25 16 01	521		12 ± 7
	13 46 09	+26 42 42	89		8 ± 10
	13 46 34	+26 50 25	36	51 ± 3	31 ± 9
	13 49 03	+27 19 48	-	8 ± 3	20 ± 11
	13 49 41	+25 24 17	71		7 ± 6
A399/A401	02 53 51	+13 22 25	325	342 ± 17	235 ± 8
	02 55 24	+13 40 10	32*		36 ± 4
	02 55 47	+13 22 19	37	52 ± 3	29 ± 4
	02 56 01	+11 31 00	84		54 ± 9
	02 56 52	+13 42 59	35	66 ± 3	26 ± 5
	02 57 25	+11 25 45	60		55 ± 4
	02 58 34	+13 03 53	28	17 ± 3	13 ± 6
	02 59 48	+12 07 18	305		107 ± 9
	03 00 23	+12 57 22	80		97 ± 7
A478	04 08 52	+08 35 38	190		61 ± 12
	04 10 55	+11 04 43	836		395 ± 9
	04 11 02	+10 10 19	-	14 ± 3	7 ± 4
A2142	15 48 08	+27 27 02	166		58 ± 7
	15 52 28	+27 55 35	61		2 ± 6
	15 58 04	+27 11 13	163		5 ± 6
	15 58 57	+26 53 35	-	56 ± 3	17 ± 6
	16 00 03	+26 18 43	57		38 ± 6
	16 00 35	+26 54 15	498		176 ± 14
	16 04 54	+27 25 22	326		186 ± 17
A2244	16 53 50	+32 48 55	88		48 ± 6
	16 56 12	+34 48 01	512		297 ± 11
	17 06 12	+33 50 37	110		95 ± 8

4.1.5 A2142: Map (e)

The 7.5σ detection of A2142 appears to be relatively free from bright primordial features.

4.1.6 A2244: Map (f)

A2244 does not appear in the map. Again, we suggest that the cluster may be coincident with a peak in the CMB.

4.2 Cluster Model

In the SZ effect, incident CMB photons are Compton scattered by the hot gas in a cluster's potential well. At frequencies less than 217 GHz, a brightness temperature decrement in the microwave background is observed. This is proportional to the 'Comptonisation parameter'

$$y = \frac{\sigma_{\rm T}}{m_{\rm e}c^2} \int n_e k T dl, \qquad (1)$$

which is proportional to the line integral of pressure through the cluster. This can be calculated from modelled gas density distributions.

As we are working with specifically large–angular scale SZ data, contamination from primordial CMB features is considerable, thus adding an extra 'noise' term. (In our parameter inference, this is dealt with appropriately as an additional source of Gaussian noise - see section 4.4). This restricts us to a highly constrained, simple model. We choose to follow Grego et al. (2001) in fitting a β–model (Cavaliere & Fusco-Femiano (1976), Cavaliere & Fusco-Femiano (1978)) to the cluster visibili-

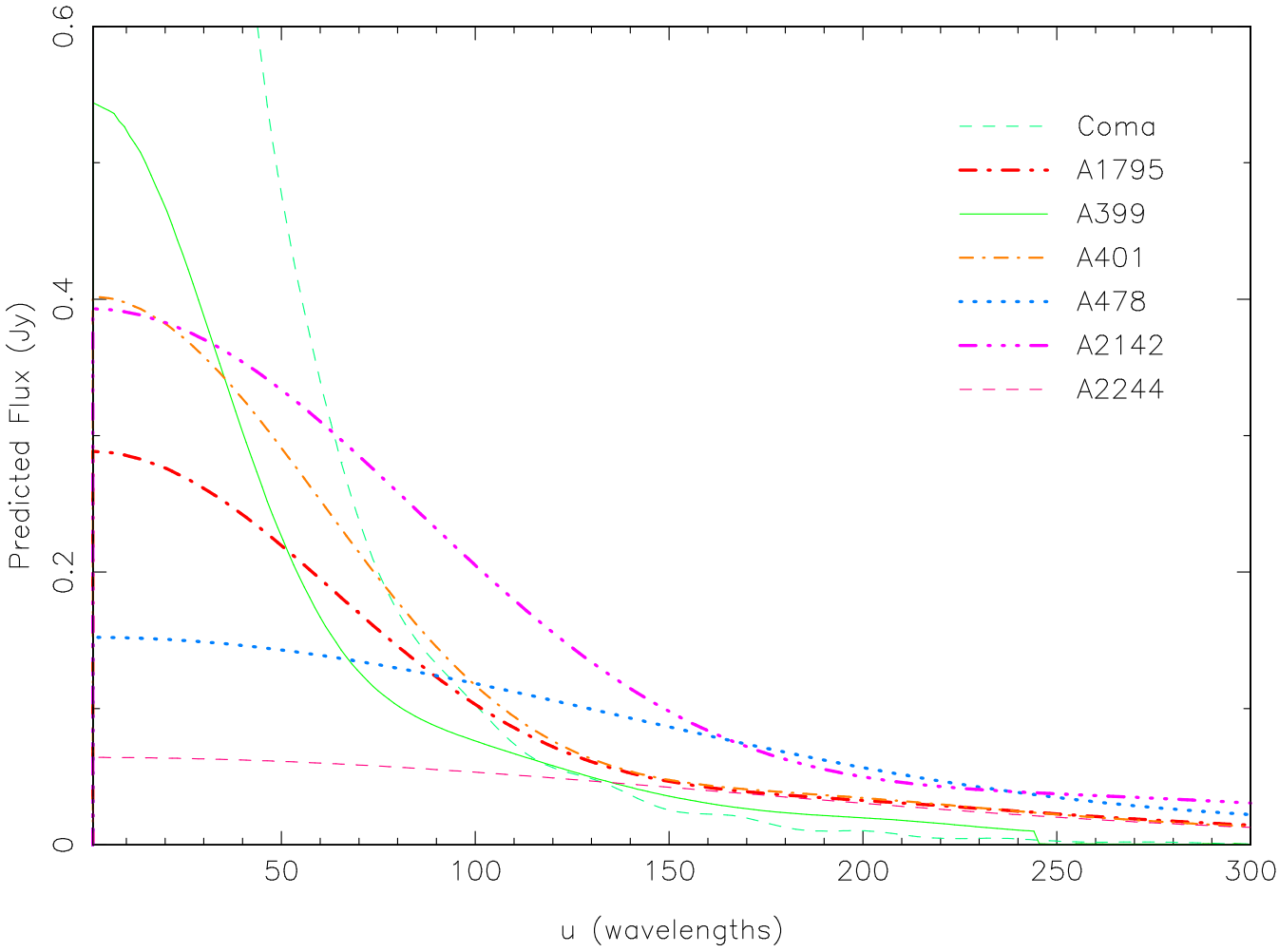

Figure 1. Predicted SZ profiles for the cluster sample.

ties. We too simplify the problem by assuming the clusters to be spherically symmetric and in hydrostatic equilibrium. (Note: Strictly the assumptions of isothermality, β–profile, and hydrostatic equilibrium are incompatible. However, to good approximation, they are compatible over a wide range of r for β close to 2/3. See King (1962).) In the β–model, the gas density as a function of radius takes the form

$$\rho_{\rm gas}(r) = \frac{\rho_{\rm gas}(0)}{\left(1+(r/r_{\rm c})^2\right)^{\frac{3\beta}{2}}}, \qquad (2)$$

where $r_{\rm c}$ (core radius) and β are parameters of the fit. From the assumptions of hydrostatic equilibrium and gas isothermality at temperature T,

$$\frac{kT}{\mu}\frac{d\rho_{\rm gas}}{dr} = -\rho_{\rm gas}\frac{GM_{\rm r}}{r^2}, \qquad (3)$$

where $M_{\rm r}$ is the total mass internal to r, μ is the mass per particle, and k and G are the Boltzmann and gravitational constants. Equations (2) and (3) lead to the following expression for the total mass distribution:

$$M_{\rm r} = \frac{3\beta r^3}{(r_{\rm c}^2+r^2)}\frac{kT}{\mu G}. \qquad (4)$$

This can be adapted usefully to calculate cluster masses out to some overdensity, e.g. r_{200}.

$$M_{200} = \frac{4\pi}{3}r_{200}^3(200\rho_{\rm crit}) \qquad (5)$$

$$= \frac{3\beta r_{200}^3}{(r_{\rm c}^2+r_{200}^2)}\frac{kT}{\mu G} \qquad (6)$$

In this work, we choose to calculate quantities out to r_{200} as this is a good approximation to the virial radius of a cluster. Previous studies have used r_{500} so we have also extended our calculations to produce results to this radius for comparison purposes.

From the gas density distribution (2) it is straightforward to compute the gas mass to this radius:

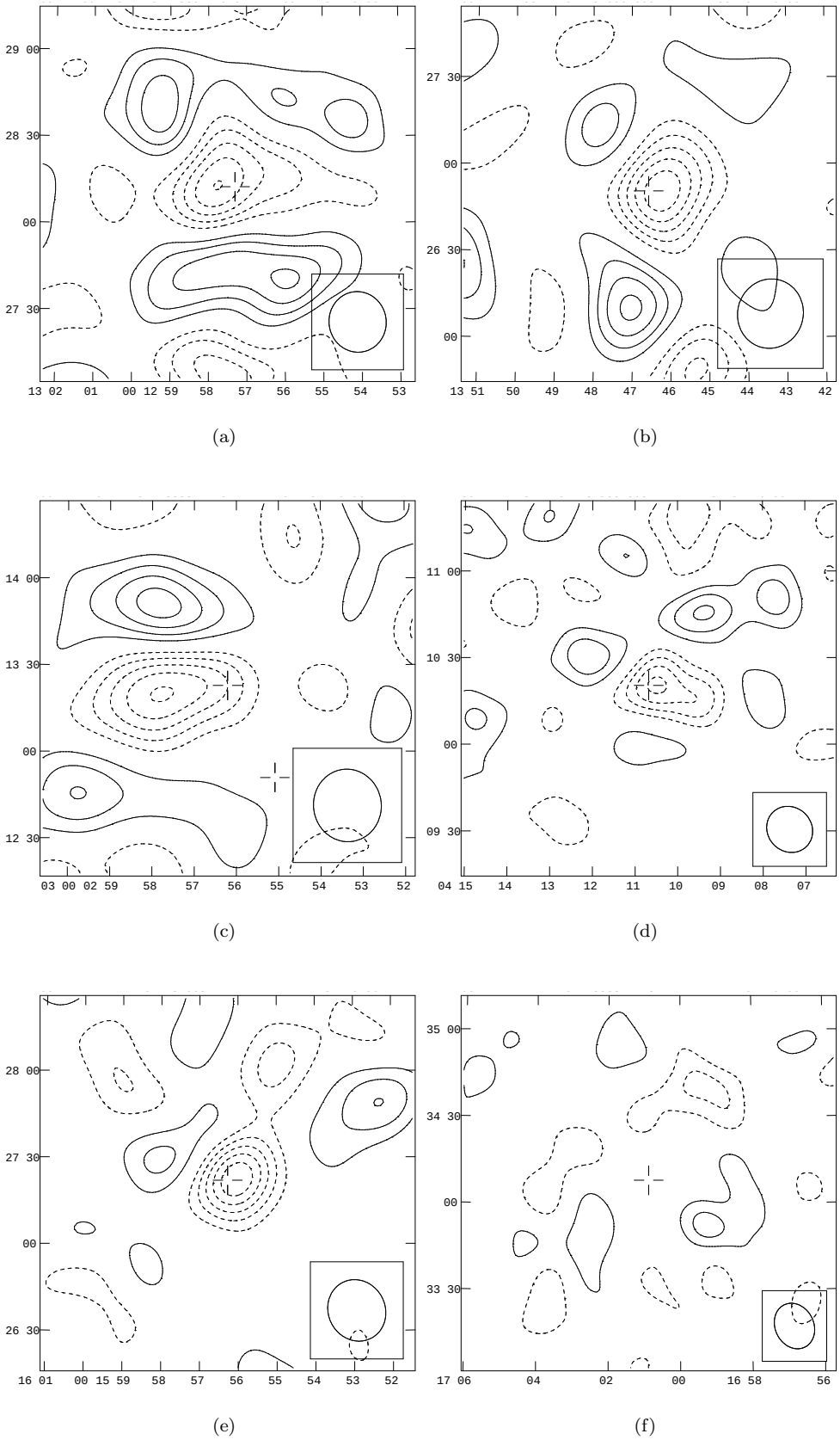

Figure 2. CLEANed VSA maps ((a)–(f)) of the clusters Coma, A1795, A399/A401 (where A399 is furthest south), A478, A2142 and A2244. The X–ray centre is marked in each case. The half–power CLEAN beam is shown in the bottom right corner of each plot, contours are 1.5σ. Radio sources have been subtracted and the coordinates are B1950.

$$M_{\rm gas} = \int_0^{r_{200}} 4\pi r^2 \rho_{\rm gas} dr \quad (7)$$

$$= 4\pi\rho_{\rm gas}(0) r_{\rm c}^3 \int_0^{\frac{r_{200}}{r_{\rm c}}} \frac{x^2 dx}{(1+x^2)^{\frac{3\beta}{2}}}. \quad (8)$$

The above integral is evaluated numerically. We choose to parameterise in terms of $M_{\rm gas}$, and can solve for the gas density in order to compute the Comptonisation parameter. The calculated values can then be compared to real VSA data.

The gas fraction is defined as

$$f_{\rm gas} = \frac{M_{\rm gas}}{M_{\rm r}}, \quad (9)$$

in which $M_{\rm gas}$ and $M_{\rm r}$ are evaluated to the same radius. $f_{\rm gas}$ evaluated by this method is proportional to h^{-1}. One way to see this is as follows. In equation 8, the h–dependences of the limit $r_{200}/r_{\rm c}$ cancel, $\rho_{\rm gas}(0)$ is a local quantity and so not h–dependent, and only $r_{\rm c}^2$ depends on h because the third factor of $r_{\rm c}$ is along the line of sight; thus $M_{\rm gas} \propto h^{-2}$. In equation 4, $M_{\rm r} \propto r^3/(r_{\rm c}^2 + r^2) \propto h^{-1}$. So, $f_{\rm gas} \propto h^{-1}$.

4.3 Interferometric Data

Interferometers sample the uv–plane so it follows that the most straightforward approach is to fit to the visibility data directly. This is further motivated by the following points. The instrument noise is Gaussian in the uv–plane, and independent between visibilities. In the map plane the noise is highly correlated spatially. In addition, fitting to the visibilities naturally avoids the problem of synthesised beam deconvolution. The primordial CMB is well understood in the uv–plane in terms of the measured power spectrum, so can be factored into the computation (see 4.4 for details). Finally, the inclusion of point sources is straightforward.

4.4 Contaminants

There are two relevant astrophysical contaminants to the SZ data: primordial fluctuations in the CMB, and foreground radio sources. Emission from the Galaxy is taken to be negligible in this analysis.

Primordial CMB fluctuations, recognised as a source of Gaussian noise with known angular power spectrum, are included in a non-diagonal covariance matrix when calculating the misfit between predicted and observed data (Reese et al. (2002), Marshall et al. (2003)). We observed bright primordial features in all of our cluster maps, and indeed they are evident in Figure 2. As the negative primordial features are of similar strengths and on similar angular scales to the cluster decrements, it is necessary to apply fairly tight positional priors (see section 4.5). As regards $f_{\rm gas}$ estimates, we argue that the position is acceptable as the effect of the CMB tends to produce a cancelling effect on $M_{\rm gas}$ and $M_{\rm r}$ (see section 4.6).

The point sources present in each field are also included in the model of the sky. The source–subtractor data allow the determination of the fluxes and positions of these objects: we translate these measurements into appropriate priors (see section 4.5) on the source parameters. These 'nuisance parameters' are then marginalised out.

4.5 Parameter Inference

4.5.1 Basic considerations

In inferring cluster parameters, the traditional route followed in the literature is the Maximum Likelihood method. This method was used in, for example, the SZ and gas fraction work of Grego et al. (2001). Computational restrictions at the time prevented the use of the fully Bayesian analysis we perform in this paper. The likelihood of a dataset $\mathrm{L(data}|\boldsymbol{\theta})$ is the product of the probability distributions of the constituent data points, where $\boldsymbol{\theta}$ is used to characterise a set of parameters such as β and core radius. This likelihood may be maximised to find the best–fit value for each parameter of the set $\boldsymbol{\theta}$. This approach:

(i) assumes that the parameters $\boldsymbol{\theta}$ of a model have a true set of values, and that obtaining data from an appropriate experiment will measure this set of values;

(ii) can be formulated in terms of a single misfit statistic when describing the difference between the predictions of a model and a measurement: maximising a Gaussian likelihood for data with uncorrelated errors is equivalent to minimising the mean–squared residual, or chi-squared statistic;

(iii) usually assumes Gaussian noise, although indeed this can be modified to incorporate the correct distribution (e.g. Poisson) for a particular case.

The Maximum Likelihood method focuses on the estimation of true parameters from data, while neglecting the full distributions for those parameters. When signal–to–noise is low, these distributions are broad and very unlikely to be Gaussian: we summarise the difficulties in this situation as follows.

Maximum Likelihood does not describe the joint process of observation and inference. We have a set of noisy visibilities (the data) which we attempt to explain by a model or hypothesis, H. The hypothesis includes the notions, for example, that the SZ signal comes from a gas distribution (which we assume here to have a β–profile) and that sources and CMB primordials are present, and also the assumption that we understand the experiment in question (i.e. the interferometer works). The data model includes the parameter set $\boldsymbol{\theta}$ as defined above. We wish to estimate $\boldsymbol{\theta}$ from our data, that is, we wish to examine the probability distribution $\mathrm{P}(\boldsymbol{\theta}|\mathrm{data, H})$. N.B.: the notation P(A|B) refers to the probability of A given B. Rather than achieving this, the Maximum Likelihood method assesses the data while taking it as *given* that $\boldsymbol{\theta}$ has some true value, as outlined in point (i) above. In other words, it evaluates just the peak of the probability distribution $\mathrm{P}(\mathrm{data}|\boldsymbol{\theta}, \mathrm{H})$. Application of Bayes' theorem allows us to relate the two distributions $\mathrm{P}(\boldsymbol{\theta}|\mathrm{data, H})$ (the *posterior*) and $\mathrm{P}(\mathrm{data}|\boldsymbol{\theta}, \mathrm{H})$ by

$$\mathrm{P}(\boldsymbol{\theta}|\mathrm{data, H}) = \frac{\mathrm{P}(\mathrm{data}|\boldsymbol{\theta}, \mathrm{H})\mathrm{P}(\boldsymbol{\theta}|\mathrm{H})}{\mathrm{P}(\mathrm{data}|\mathrm{H})}. \quad (10)$$

The additional factors in equation 10 are the *prior* probability distribution, $\mathrm{P}(\boldsymbol{\theta}|\mathrm{H})$, and the *evidence*, P(data|H), to which we will return shortly.

In addition, point (ii) is not generally correct. Even if $\mathrm{P}(\mathrm{data}|\boldsymbol{\theta},\mathrm{H})$ is Gaussian, it is multiplied by the prior $\mathrm{P}(\boldsymbol{\theta}|\mathrm{H})$ which may, for example, be asymmetric. Once one starts to produce resultant probability density functions by multiplication the distributions are certainly going to be complicated. The probabilities outlined above are *functions*. The standard Maximum Likelihood approach characterises such probability distributions by a single value with an error bar. The characterisation of probability distributions with approximate Gaussians is therefore misleading and may underestimate the final uncertainty in a quantity such as $\mathrm{f_{gas}}$. It is clearly preferable to retain all the information contained in the entire function, rather than working with single–value parameters. As mentioned above, point (iii) can be dealt with appropriately.

Propagating the likelihood function via Bayes' theorem thus overcomes points (i) and (ii) above. It also delivers additional advantages, summarised as follows:

- Conditioning on a particular value of a parameter implies a delta–function prior, a state of knowledge that never occurs. It is now possible to deal with continuous probability distribution functions in many dimensions (e.g. positions, core radii, M_{r} etc.) rather than having to work just with peaks and widths of artificially low–dimension probability distributions. A desire to concentrate on a subset of interesting parameters leads directly to the concept of marginalisation (see e.g. Sivia (1996)) .
- The method leads directly to the evaluation of the evidence, an extremely useful quantity that enables one to assess the relative suitability of a set of hypotheses (see e.g. Hobson et al. (2002)).

The evidence in Equation (10) is $\mathrm{P}(\mathrm{data}|\mathrm{H})$ and is an integral over all parameters in N–dimensional parameter vector $\boldsymbol{\theta}$:

$$\mathrm{P}(\mathrm{data}|\mathrm{H}) = \int \mathrm{P}(\mathrm{data}|\boldsymbol{\theta},\mathrm{H})\mathrm{P}(\boldsymbol{\theta}|\mathrm{H})\mathrm{d}^{\mathrm{N}}\boldsymbol{\theta} \qquad (11)$$

This can be applied usefully to help distinguish between different hypotheses, say $\mathrm{H_1}$ and $\mathrm{H_2}$: Bayes' theorem (equation 10) can be applied in order to evaluate and compare $\mathrm{P}(\mathrm{H_1}|\mathrm{data})$ and $\mathrm{P}(\mathrm{H_2}|\mathrm{data})$. In doing this, $\mathrm{P}(\mathrm{data})$ cancels out and we obtain

$$\frac{\mathrm{P}(\mathrm{H_1}|\mathrm{data})}{\mathrm{P}(\mathrm{H_2}|\mathrm{data})} = \frac{\mathrm{P}(\mathrm{data}|\mathrm{H_1})}{\mathrm{P}(\mathrm{data}|\mathrm{H_2})}\frac{\mathrm{P}(\mathrm{H_1})}{\mathrm{P}(\mathrm{H_2})} \qquad (12)$$

Thus hypotheses may be compared. For example, we can evaluate the hypothesis that an SZ cluster is in a particular, small patch of sky. We can compare this with the evidence given an alternative hypothesis, this time deeming that the cluster be found in a larger area of sky. The hypothesis probability ratio given in equation 12 provides the means by which the suitability of these two priors can be assessed. Such additional information may be obtained from elsewhere; in this particular example X-ray data may be used to good effect.

We note that both Maximum Likelihood and Bayesian methods can cope with correlated data (See e.g. Marshall et al. (2003), Reese et al. (2002) as before) but simple chi-squared minimisation cannot.

4.5.2 Characterising the posterior Probability Density Function (PDF)

Having summarised the advantages of the Bayesian route, we now turn to the problem of calculating the posterior distribution $\mathrm{P}(\boldsymbol{\theta}|\mathrm{data},\mathrm{H})$. One method is to evaluate it as a product of the probabilities for every visibility, for all possible values of each of the N parameters in $\boldsymbol{\theta}$. This is the 'brute force' approach, involving the calculation of the likelihood over a huge hypercube. This technique is now plausible for application to the CMB primordial power spectrum, given that the CMB itself has a Gaussian brightness probability distribution at every point on the sky (and is indeed the same everywhere). However, it is not a realistic approach for an SZ β–model with position, mass and size uncertainties in the presence of the CMB and a number of radio sources. So we have chosen to represent the posterior in an approximate way by drawing samples from it, the Markov Chain Monte Carlo method (see e.g. Gilks et al. (1996), Ó Ruanaidh & Fitzgerald (1996) for general introductions, and Marshall et al. (2003), Bonamente et al. (2004) for galaxy cluster specifics).

This process results in a set of sample parameter vectors whose number density is proportional to the posterior probability, such that all local maxima are explored in proportion to their relevance. In order to ensure that the correct regions of parameter space are being probed, sufficient samples must be taken and calculations made. This is problematic in that it must be both accurate and efficient: to this end, we use the commercially available sampler '`BayeSys`' (Skilling (2002)), a powerful code designed to be flexible enough to cope with a wide range of problems. `BayeSys` makes use of a range of proposal distribution 'engines' that govern where next to sample, and in particular employs those that it finds dynamically to be most efficient for a particular posterior pdf. In addition, it should be possible to assess whether or not enough evaluations have been performed over an acceptable range of $\boldsymbol{\theta}$, that is when the process has 'burnt in'. A review of such tests is given in Cowles & Carlin (1996). We follow Marshall et al. (2003) and argue that several short, independent burn–ins are a good idea to check that they agree. The diagnostic we use is the evidence itself, which we calculate by 'Thermodynamic Integration' (see e.g. Ó Ruanaidh & Fitzgerald (1996)). The method works as follows. The evidence (as given in equation 11) is

$$\mathrm{P}(\mathrm{data}|\mathrm{H}) = \int \mathrm{P}(\mathrm{data}|\boldsymbol{\theta},\mathrm{H})\mathrm{P}(\boldsymbol{\theta}|\mathrm{H})\mathrm{d}^{\mathrm{N}}\boldsymbol{\theta} \equiv \mathrm{E}(1) \qquad (13)$$

.

We now write down

$$\mathrm{E}(\lambda) = \int \mathrm{P}^{\lambda}(\mathrm{data}|\boldsymbol{\theta},\mathrm{H})\mathrm{P}(\boldsymbol{\theta}|\mathrm{H})\mathrm{d}^{\mathrm{N}}\boldsymbol{\theta} \qquad (14)$$

.

`BayeSys` allows the running in parallel of several Markov chains (typically 10 in our case). The key to the method is as follows. The sampling starts with $\lambda = 0$. This means that the new data are initially ignored with samples just being drawn from the prior. At this stage, remote regions of parameter space (that are at least allowed by the prior) are sampled. λ is then gradually raised to one, at a rate

balancing the needs for computational speed and accuracy in the log evidence calculation. The latter can be shown to reduce to the numerical integral of the ensemble–averaged log–likelihood with respect to λ (Ó Ruanaidh & Fitzgerald (1996)).

4.5.3 Practicalities

It is always of utmost importance to ensure that one does not over–interpret the data available. This is crucial here, as we have not only fairly noisy data (due to the faint nature of the effect being studied), but also considerable contamination from point sources and primordial CMB fluctuations. As is evident in the VSA data (figure 2), and previously mentioned in section 4.4, CMB features may be comparable in strength to the SZ decrement itself. It would be quite possible to fit, accidentally, to a negative CMB feature which would be very misleading. Our method avoids this danger by including all contaminants in the model, and fitting all parameters simultaneously. We have chosen to fit a simple but well–motivated model to our data, but even so we must fit six parameters plus source fluxes and positions. This makes the task computationally expensive (vastly more so than using Maximum Likelihood). In order to extract parameters for a single cluster, around 100 hours of computer time is required (2 GHz processor). We do not expect to place tight constraints on, for example, β or $r_{\rm c}$ and we anticipate broad probability distributions for all parameters. However, when we marginalise properly over all parameters we find some interesting precisions on $f_{\rm gas}$.

In order to compare a sample model with the VSA data, we project the model gas pressure and map the Comptonisation onto a grid. A Fast Fourier Transform is then performed, and interpolated onto the $u-v$ coordinates. These predicted visibilities are then compared to the observed cluster visibilities. Working directly with the visibilities has the advantages described in section 4.3. We deal with point sources and the CMB in the following natural way. The Fourier transform of a delta function is a constant amplitude sine wave. This can be used to increment all the predicted visibilities by a factor specific to each source's sample parameters. The uncertainty on each measured visibility is Gaussian and has contributions from both the thermal noise in the receivers (which is uncorrelated) and the primordial CMB fluctuations (which are correlated between adjacent points in the $u-v$ plane). The resultant noise covariance matrix C is non-diagonal but calculable given a primordial power spectrum, assumed to be well known. The likelihood of the visibility data is therefore

$$\mathrm{P}(\boldsymbol{d}|\boldsymbol{\theta},\mathrm{H}) = \frac{1}{(2\pi)^{\mathrm{N_{vis}}}|\mathsf{C}|^{1/2}} \exp\left[-(\boldsymbol{d}-\boldsymbol{d_p})^{\mathrm{T}}\mathsf{C}^{-1}(\boldsymbol{d}-\boldsymbol{d_p})\right], \quad (15)$$

where $\boldsymbol{d}$ and $\boldsymbol{d_p}$ represent the observed and predicted visibility vectors respectively, and $N_{\rm vis}$ is the number of visibilities.

The priors used to characterise the various model parameters are summarised in Table 3. As mentioned in section 4.4, tight priors were placed on both the cluster position, and point source positions and fluxes. For the cluster centroid, the X-ray centre (Böhringer et al. (2000)) was included as a Gaussian prior of width 1 arcmin. We chose to place a weak prior on core radius such that it be determined by the data to hand. The prior on the β parameter encompasses the extremes of the range of values found in clusters to date. The temperature prior allows a generous error on the fit. Note that $f_{\rm gas}$ depends on T^2 – see Grego et al. (2001). The prior on the gas mass more than encompasses the accessible range. The point source fluxes included in the model were also assigned Gaussian priors, based on the source–subtractor measurements and their uncertainty. The prior on each source flux was broadened to account for variability of a factor of 1.33 times the measured flux: this step was only taken when the epoch of the source measurement was significantly different from that of the cluster observation. For the sources selected using predictions from lower frequencies, positional accuracies were taken from the GB6 catalogue. The sources detected in the RT surveys were assumed to have positional uncertainty of ± 40 arcsec in both RA and Dec; this is wide enough to cover even the weakest sources.

Table 3. Priors for the cluster analysis. Positions and gas temperatures for individual clusters are quoted in Table 1.

Parameter	Prior
Position	Gaussian, 1 arcmin
$r_{\rm c}$	Uniform, 1–1000kpc
β	Uniform, 0.3–1.5
$T_{\rm e}$	Gaussian, ASCA value $\pm 15\%$
$M_{\rm gas}$	Uniform, $(0.01-3.00)\times 10^{14}$

4.6 The Effect of Primordials on $f_{\rm gas}$ Estimates

In the context of large angular scale SZ observations, the CMB is additional noise which will provide a source of error in the determination of $f_{\rm gas}$. This extra noise was dealt with correctly when calculating cluster parameters (see Section 4.4). However, here we present a simple argument describing why, in situations where the SZ data is used to infer *both* the gas mass *and* the total mass (as discussed in 4.2), the contamination is not as catastrophic as one may anticipate. With the present data quality, fitting a β–model is doing little more than fitting an offset plus a slope. If there is more negative signal due to a negative CMB feature coinciding with the cluster position, then the $M_{\rm gas}$ estimate will be higher. (NB: This is a simplistic argument because of course the contribution to the Comptonisation parameter depends on the mass distribution which is linked to the total mass.) Now, in estimating $M_{\rm r}$, the effect of the above will be to increase the central concentration, increasing β or decreasing $r_{\rm c}$. Examination of Equation 8 shows that this effect will increase an estimation of $M_{\rm r}$. So, in this type of scenario, as both $M_{\rm gas}$ and $M_{\rm r}$ will be higher, the effects of the CMB tend to cancel out when calculating $f_{\rm gas}$ for the cluster in question. A similar effect is observed for a bright primordial feature - the SZ signal will tend to decrease, and β will also decrease as the cluster will appear to be less centrally condensed. Thus, if the primordial CMB contamination happens to be correlated over the measured u–range, then the effects on $M_{\rm gas}$ and $M_{\rm r}$ tend to cancel, leaving $f_{\rm gas}$ little affected.

In general, depending on the actual sizes, shapes and positions of the primordial features behind the SZ decrement, $f_{\rm gas}$ may be pushed higher or lower, or remain relatively unaffected as outlined above. Of course, if there is

Table 4. Gas fraction estimations for A478 with the inclusion of a test contaminant source of flux S_{add} at the cluster centre.

$S_{\rm add}$ (mJy)	$f_{\rm gas}$
-100	$0.056^{+0.088}_{-0.041}$
-50	$0.10^{+0.12}_{-0.06}$
-25	$0.12^{+0.14}_{-0.07}$
0	$0.12^{+0.11}_{-0.06}$
25	$0.13^{+0.14}_{-0.07}$
50	$0.11^{+0.13}_{-0.06}$
100	$0.10^{+0.09}_{-0.05}$

a Universal value of $f_{\rm gas}$, then combining the results from a reasonable number of clusters will both help reduce any remaining effects and also help to evaluate the effect's magnitude. One may intuitively regard the cases presented above to be the 'worst case scenario', when in fact they appear not to cause too great a difficulty.

We have performed a simple simulation in order to examine this cancelling effect semi–quantitatively. Using our A478 data, we placed a test source of flux $S_{\rm add}$ at the pointing centre and re–calculated $f_{\rm gas}$. Results for test sources in the range $-100 > S_{\rm add} > 100$ mJy are presented in Table 4. Although this is by no means a rigorous test of the argument postulated, we note that the values of $f_{\rm gas}$ for all $S_{\rm add}$ are consistent within errors. This indicates that in this context (ie for our uv–range and chosen cluster sample), the effect of the CMB tends to cancel out in this context. Note that typical SZ fluxes are $\approx$150 mJy, whereas CMB plus receiver noise will typically produce features of $\approx$100 mJy, and occasionally >150mJy. From these simple calculations, we argue that estimations of $f_{\rm gas}$ should be relatively unaffected by the presence of primordial CMB in all but the worst cases.

4.7 Other Effects on $f_{\rm gas}$

In this work, the random errors present are larger than any systematics, but here we present a brief discussion of some possible additional sources of error. Our assumptions of isothermality and sphericity may affect our inferred values for $f_{\rm gas}$. If a cluster were not isothermal, we may, for instance, overestimate the temperature in the outer regions due to a temperature gradient, and may overestimate both the gas and total mass with a possible small net underestimate of the gas fraction. Regarding asphericity, which we do not expect to have a large effect since we are not using X-ray surface brightness, we point out that our sample is orientation unbiased, because our flux limit is well above the flux limit of the X-ray survey from which the clusters were chosen. Grego et al. (2001) made mock observations of a simulated cluster population, finding no bias as a result of using a spherical isothermal β–model, suggesting that these two sources of systematic error indeed may not be significant in this work. Additionally, Arnaud et al. (2004) find that the temperature variation for clusters observed with XMM-Newton is less than 10% out to half the virial radius, and similarly Zhang et al. (2004) find errors on mass estimates from XMM-Newton data to be less than 25% as a result of temperature gradients. Generally, X-ray derived pressure maps seem to show a factor of two less variation, for example azimuthally around the cluster centre, than either density or temperature maps. Still, gas clumping could be a problem. Clumps, if unresolved, will lead to enhanced signal in an X-ray map and thus bias the cluster temperature. This will artificially increase the inferred total mass. However, the SZ data themselves are less sensitive to clumping as the SZ signal is proportional to $n_{\rm e}$ rather than $n_{\rm e}^2$. Ultimately, the comparison of high signal–to–noise SZ data with X-ray measurements will constrain the level of clumping in clusters.

4.8 Cluster Parameters

We discuss the constraints placed on core radius and β–parameter by the VSA data, and also present results for the gas mass, total mass and gas fractions calculated out to both r_{200} and r_{500}. For comparison, a summary of cluster parameters derived from X-ray data is presented in Table 5.

We find, as anticipated, that the cluster parameters β and $r_{\rm c}$ are poorly constrained by the SZ data, as shown in Figure 3. For Coma, A1795, A478 and A2142 there is considerable degeneracy between the two parameters. It is only possible to place limits on the two parameters together – little can be said about them as separate entities. This is largely due to the limited range of angular scales presented in this data, and indeed in any SZ data to date. Ideally, one would combine the VSA data with observations on smaller angular scales. This is impossible in this case, as instruments such as the RT would completely resolve out signal from the clusters in our sample. AMI (see e.g. Kneissl et al. (2001)) will work over a larger range of angular scales and should start to break this degeneracy. A401, A399 and A2244 are not detected in the cluster maps, so it is perhaps unsurprising that little constraint can be placed upon the shape parameters by these data.

We present the median of the probability distribution for the gas mass, total mass and gas fraction for each cluster, evaluated to both r_{200} and r_{500}, in Table 6. The errors quoted are the values of the $16.5^{\rm th}$ and the $83.5^{\rm th}$ percentiles. We note that A1795, A478 and A2142 all favour a gas mass of around $10^{14} M_{\odot}$. The Coma data allow very high gas masses. This may be interpreted as the cluster position coinciding with a negative feature in the CMB, thus making the SZ decrement appear deeper. The converse may be true for the other three clusters, in that their SZ signals may be partially 'obscured' by hot spots in the CMB. If this were true it would have the effect of reducing the preferred values of the gas mass, and indeed these objects do allow low values of this parameter. (Note: although here we choose to follow Myers et al. (1997) in using X-ray temperatures from Markevitch et al. (1998), we recognise that more recent data are available. Repeating the analysis using XMM-Newton temperatures (Pointecouteau et al. (2004), Sun et al. (2003)) we find that the resulting $f_{\rm gas}$ values are fully consistent with those presented in Figure 5 and Table 7. Any variations are below the random errors present in the VSA data).

It is interesting to examine the constraints placed on the relationship between total mass $M_{\rm r}$ and gas temperature by the VSA SZ data. In Figure 4 we plot the X-ray

Table 5. Cluster parameters derived from X-ray data. References are [1] Mason & Myers (2000), [2] Mohr et al. (1999), [3] Sanderson & Ponman (2003)

	r_c (arcmin)		β			n_0 ($10^{-3}h_{100}^{1/2}$cm^{-3})	($10^{-3}h_{50}^{1/2}$cm^{-3})
	[1]	[3]	[1]	[2]	[3]	[1]	[2]
Coma	9.32 ± 0.10	-	0.670	$0.705^{+0.046}_{-0.046}$	-	$4.51^{+0.04}_{-0.04}$	$3.12^{+0.04}_{-0.04}$
A1795	2.17 ± 0.28	$4.01^{+0.20}_{-0.21}$	0.698	$0.790^{+0.031}_{-0.032}$	0.83±0.02	$11.29^{+0.61}_{-1.77}$	$29.9^{+4.6}_{-1.5}$
A399	4.33 ± 0.45	$1.89^{+0.36}_{-0.36}$	0.742	-	0.53±0.05	$3.24^{+0.14}_{-0.19}$	-
A401	2.26 ± 0.41	$2.37^{+0.09}_{-0.09}$	0.636	$0.606^{+0.015}_{-0.016}$	0.63±0.01	$8.01^{+0.56}_{-1.02}$	$5.87^{+0.43}_{-0.27}$
A478	1.00 ± 0.15	$2.34^{+0.23}_{-0.23}$	0.638	$0.713^{+0.030}_{-0.033}$	0.75±0.01	$28.9^{+15.2}_{-3.9}$	$38.1^{+3.3}_{-1.5}$
A2142	1.60 ± 0.12	$3.14^{+0.22}_{-0.22}$	0.635	$0.787^{+0.082}_{-0.093}$	0.74±0.01	$15.03^{+0.92}_{-1.07}$	$15.8^{+1.7}_{-2.4}$
A2244	0.82 ± 0.14	-	0.580	$0.594^{+0.061}_{-0.045}$	-	$17.73^{+1.95}_{-2.65}$	$13.2^{+1.9}_{-2.9}$

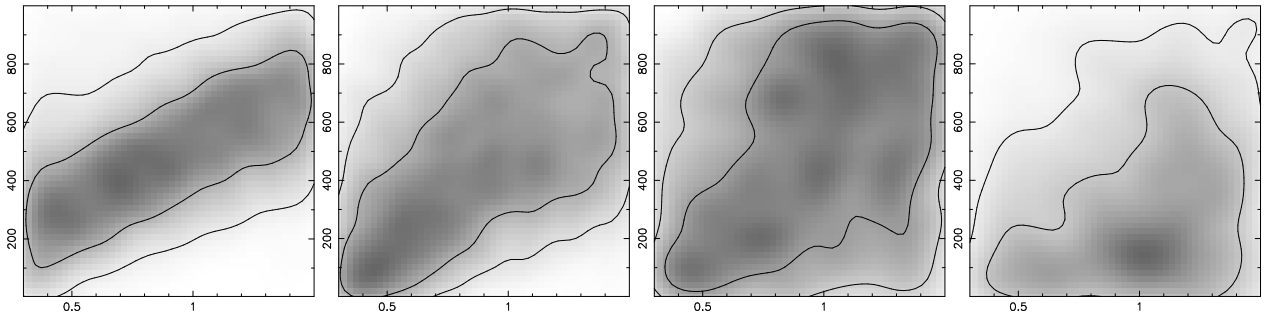

(a)Coma (b)A1795 (c)A399 (d)A401

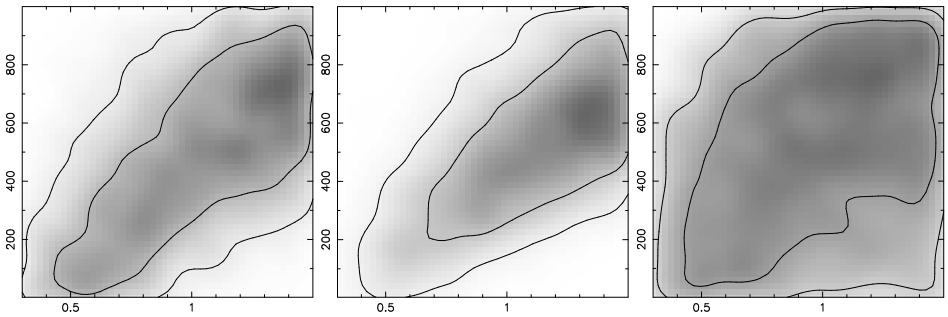

(e)A478 (f)A2142 (g)A2244

Figure 3. Plots illustrating the constraints placed on β–parameter and core radius by the cluster data. In each plot, the x-axis is β and the y-axis is core radius (kpc). 68% and 90% contours are shown.

determined temperature and the total mass M_r derived using equation 6. We expect, of course, some scatter on the values of M_r for each cluster due to the CMB contamination of the SZ data. After examination of equation 6, we argue that the normalisation of our $M-T$ relation is in fact mainly determined by the profile fitting parameters β and r_c derived from the VSA data, and depends only weakly on T_X ($T_X^{-1/2}$ for the self–similar 3/2 slope of the M-T relation.) This means in Figure 4 that the effect of any uncertainty in T (and consequently in M_{500}) for a given set of β, r_c from the VSA will move the data points within their large error boxes almost parallel to the slope of the $M-T$ relation. For comparison we plot the normalisation of the $M-T$ relations from hydrodynamical adiabatic simulations (Evrard et al. (1996)) and X-ray cluster data (Finoguenov et al. (2001)). We calculate our normalisation constant for $M \propto T^{3/2}$ to be $2.33^{+0.85}_{-0.78} \times 10^{13}$. This is in good agreement with the recent $M-T$ determinations derived from X-ray data (Allen et al. (2001), Pratt & Arnaud (2002)). In a forthcoming paper we intend to investigate the possibility of determining the $M-T$ relation from SZ without the use of an X-ray temperature. Such an $M-T$ relation, based on a measurement of the global gas pressure distribution via the SZ effect, will be interesting to contrast with X-ray measurements. This kind of work will be very useful for the interpretation of upcoming SZ cluster surveys.

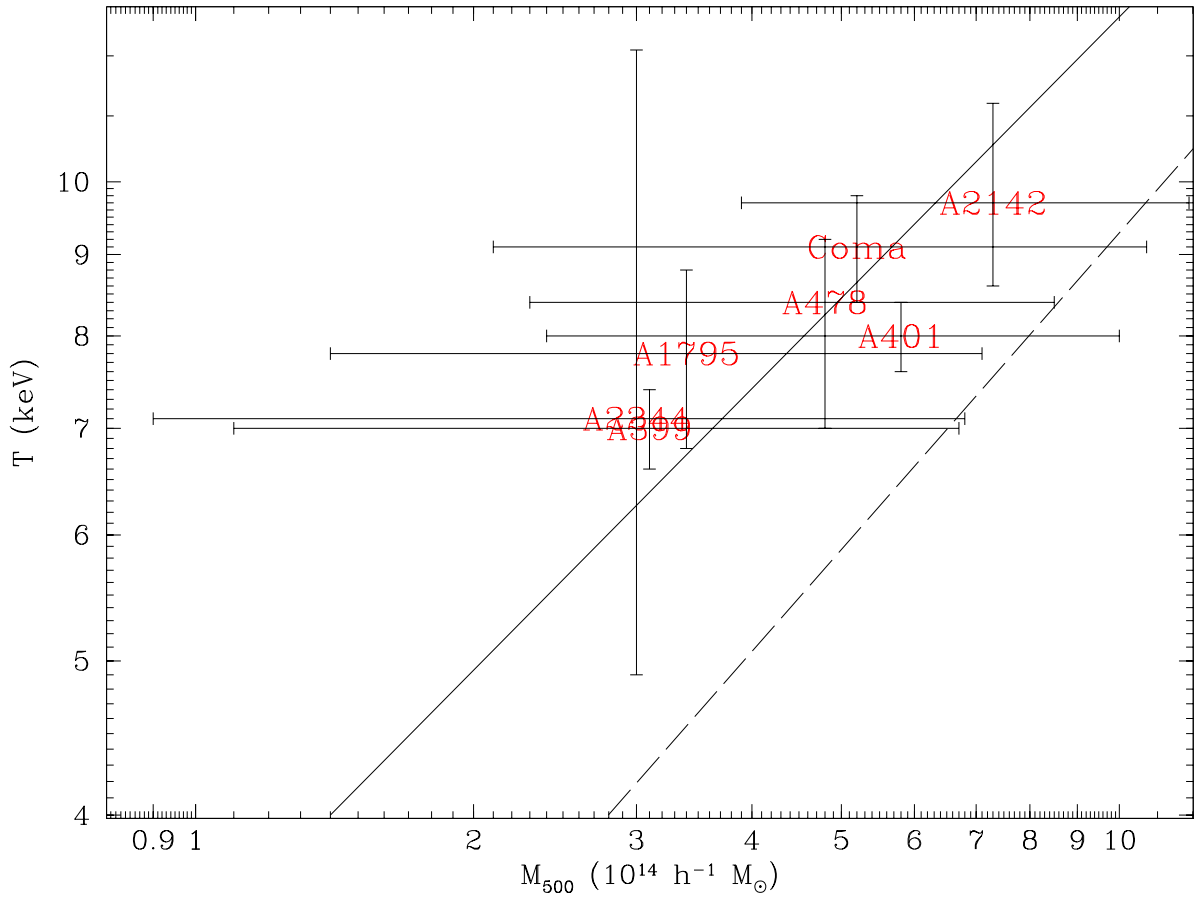

Figure 4. The mass–temperature scaling relation derived from fitting gas pressure profiles to the VSA SZ data. The temperature shows the X-ray temperatures given in Table 1 and also enters M_{500} linearly. The dashed line uses the normalisation from hydrodynamical adiabatic simulations (Evrard et al. (1996)), and the solid line represents the best fit $M-T$ relation of Finoguenov et al. (2001).

The $f_{\rm gas}$ probability distributions are highly non-Gaussian, and are plotted on the same axes in Figure 5. The errors quoted are the values of the $16.5^{\rm th}$ and the $83.5^{\rm th}$ percentiles. In order to compare values for individual clusters, we summarise results from other experiments in Table 7.

We have combined the posterior probability density functions for each cluster gas fraction as follows (see Marshall (2004), in preparation, for more details). Simulating the effect of simultaneously fitting all our SZ data with the same global gas fraction $f_{\rm gas}$ requires dividing out the prior on the individual cluster gas fraction (which can be derived from a set of MCMC samples with no data, see Slosar et al. (2003)) and then multiplying the resulting effective likelihoods together. Modulating this product by the prior on $f_{\rm gas}$, which we take to be uniform over the range [0–0.2], gives us the posterior pdf P($f_{\rm gas}$|data). Moreover, keeping track of the normalisations allows us to compute a relative probability for the act of combination itself, that is, the ratio P(data|$\mathrm{H}^{\rm global}$)/P(data|$\mathrm{H}^{\rm i}$)), where $\mathrm{H}^{\rm i}$ is the hypothesis 'all clusters have independent gas fractions $f^{\rm i}_{\rm gas}$', whilst $\mathrm{H}^{\rm global}$ is the alternative hypothesis that 'all clusters have the same gas fraction $f_{\rm gas}$'.

We first assume that *all* our clusters have one true global gas fraction value, $f_{\rm gas}$. We combine the individual probability density functions for all of our clusters, including those with what would classically be called non–detections. We find $f_{\rm gas}h_{100} = 0.023^{+0.016}_{-0.012}$, with an evidence ratio in favour of this all-encompassing combination of

$$\frac{\mathrm{P(data|H^{global})}}{\mathrm{P(data|H^{i})}} = 4.4. \qquad (16)$$

We can also divide the data into two sets, those from detected clusters and those from non–detections, and again investigate the suitability of their combination. Let hypothesis $\mathrm{H}^{\rm global}_{\rm det}$ consist of the assertions that there is a global gas fraction $f_{\rm gas}$ exhibited by the detected clusters, and that there is another gas fraction–like parameter X for the non–detections; we find the following evidence ratios:

$$\frac{\mathrm{P(data(detections)|H^{global}_{det})}}{\mathrm{P(data(detections)|H^{i})}} = 0.92, \qquad (17)$$

$$\frac{\mathrm{P(data(non-detections)|H^{global}_{det})}}{\mathrm{P(data(non-detections)|H^{i})}} = 7.41. \qquad (18)$$

Table 6. Gas masses, total masses and gas fractions for the VSA cluster sample evaluated to both r_{200} and r_{500}.

Cluster	$M_{\rm gas}(r_{200})h^2$	$M_{\rm gas}(r_{500})h^2$	$M_{\rm r200}h$	$M_{\rm r500}h$	$f_{\rm gas}(r_{200})h$	$f_{\rm gas}(r_{500})h$
	$10^{13}M_\odot$	$10^{13}M_\odot$	$10^{14}M_\odot$	$10^{14}M_\odot$		
Coma	$15.4^{+9.0}_{-8.0}$	$6.6^{+3.5}_{-3.0}$	$10.9^{+10.0}_{-6.0}$	$5.2^{+5.5}_{-3.1}$	$0.15^{+0.28}_{-0.10}$	$0.15^{+0.17}_{-0.09}$
A1795	$8.5^{+3.9}_{-3.4}$	$3.5^{+1.6}_{-1.7}$	$7.9^{+6.5}_{-4.1}$	$3.4^{+3.7}_{-2.0}$	$0.12^{+0.15}_{-0.070}$	$0.11^{+0.090}_{-0.060}$
A399	$1.9^{+2.4}_{-1.3}$	$0.7^{+1.1}_{-0.6}$	$7.6^{+5.3}_{-3.9}$	$3.1^{+3.6}_{-2.0}$	$0.030^{+0.054}_{-0.022}$	$0.028^{+0.040}_{-0.020}$
A401	$5.0^{+3.0}_{-2.3}$	$3.0^{+1.4}_{-1.4}$	$10.7^{+6.0}_{-5.0}$	$5.8^{+4.2}_{-3.4}$	$0.048^{+0.074}_{-0.028}$	$0.055^{+0.055}_{-0.029}$
A478	$11.2^{+4.0}_{-4.0}$	$5.7^{+2.1}_{-2.2}$	$10.8^{+6.0}_{-5.0}$	$4.8^{+3.7}_{-2.5}$	$0.12^{+0.11}_{-0.06}$	$0.13^{+0.08}_{-0.05}$
A2142	$11.2^{+4.0}_{-3.0}$	$6.1^{+1.7}_{-1.8}$	$15.3^{+8.0}_{-6.0}$	$7.3^{+4.6}_{-3.4}$	$0.074^{+0.068}_{-0.034}$	$0.086^{+0.056}_{-0.035}$
A2244	$1.3^{+1.6}_{-0.8}$	$4.4^{+8.4}_{-3.7}$	$7.5^{+5.8}_{-3.8}$	$3.0^{+3.8}_{-2.1}$	$0.020^{+0.039}_{-0.015}$	$0.020^{+0.031}_{-0.014}$

Table 7. Gas fractions estimated within R_0 from SZ data ([1] Myers et al. (1997)), and within r_{500} from X-ray data ([2] Mason & Myers (2000), [3] Mohr et al. (1999), [4] Ettori & Fabian (1999)).

	$f_{\rm gas}h$	R_0h(Mpc)	$f_{\rm gas}h^{3/2}$	$f_{\rm gas}h_{50}^{3/2}$	$f_{\rm gas}h_{50}^{3/2}$
	[1]	[1]	[2]	[3]	[4]
Coma	0.063 ± 0.017	1.50	0.0603±0.0028	0.177±0.019	-
A1795	-	-	0.0477±0.0036	0.190±0.008	0.184 ± 0.011
A399	-	-	0.0655±0.0032	-	-
A401	-	-	$0.0794^{+0.0044}_{-0.0062}$	0.247±0.012	0.230 ± 0.013
A478	0.166 ± 0.014	0.976	$0.0760^{+0.0076}_{-0.0045}$	$0.214^{+0.012}_{-0.011}$	0.172 ± 0.023
A2142	0.060 ± 0.011	0.76	$0.0890^{+0.0064}_{-0.0091}$	$0.227^{+0.024}_{-0.017}$	0.255 ± 0.033
A2244	-	-	$0.0739^{+0.0170}_{-0.0349}$	$0.196^{+0.061}_{-0.060}$	0.204 ± 0.104

The former suggests that the data are not good enough to distinguish between the global gas fraction hypothesis and that of all four detected clusters taking independent values of $f_{\rm gas}^{\rm i}$. However, the latter points strongly towards the combination of the non-detections' gas fractions. The overall evidence ratio from this 'split sample' analysis is therefore:

$$\frac{\mathrm{P(data(all)|H_{det}^{global})}}{\mathrm{P(data(all)|H^i)}} = \frac{\mathrm{P(data(detections)|H_{det}^{global})}}{\mathrm{P(data(detections)|H^i)}} \times \frac{\mathrm{P(data(non-detections)|H_{det}^{global})}}{\mathrm{P(data(non-detections)|H^i)}} = 6.82 \quad (19)$$

This is higher than the result in (16), indicating that the split sample analysis is more appropriate. The interpretation is that the detected clusters are telling us about a global cluster gas fraction $f_{\rm gas}$, while the non–detections are telling us far more about the primordial fluctuations (inappropriately parameterised by X). Our 'headline' result is therefore that from combining the four detected clusters' gas fractions as above: $f_{\rm gas}h_{100} = 0.08^{+0.06}_{-0.04}$.

In order to address the true value of a global $f_{\rm gas}$ we need better data, which the likes of AMI (see e.g. Kneissl et al. (2001)), AMIBA (see e.g. Lo (2002)) and the SZA (see e.g. Mohr et al. (2002)) should provide. We have, however, developed and demonstrated a useful method for estimating the effect of, and for controlling, systematics. We could do even better in estimating a universal $f_{\rm gas}$ if we were able to use prior information (from X-rays and lensing) on the likely detectability in SZ of each cluster. This would require us to be able to separate the 'position' and 'existence' implicit in the priors we use; we are planning to attempt this.

We can also place formal constraints on $\Omega_{\rm m}h$ by assuming that our estimation for $f_{\rm gas}h$ is indeed the global value.

$$f_{\rm gas}h = \frac{\Omega_{\rm b}h^2}{\Omega_{\rm m}h} \quad (20)$$

Rebolo et al. (2004) infer $\Omega_{\rm b}h^2$ and h_{100} from VSA and WMAP primordial CMB data, using a flat ΛCDM model. We take these values and find $\Omega_{\rm m}h = 0.33^{+0.33}_{-0.15}$.

Another implication concerns the clumping of the cluster gas. The broad agreement here between $f_{\rm gas}$ values from X-ray and from SZ, and as discussed in e.g. Grego et al. (2001), rules out significant clumping.

5 CONCLUSION

We have investigated with the VSA Extended Array at ≈ 34 GHz the SZ effects towards seven nearby clusters that form a complete, X-ray–flux–limited sample.

(i) Four of the clusters (Coma, A1795, A478, A2142) show SZ effects in the map plane on scales of ≈20 arcmin of typically 6σ.

(ii) There is significant detection of CMB primordial structure at this resolution, which is the likely cause of the three non-detections (A399, A401, A2244).

We have analysed the data in the uv–plane, with X-ray priors on positions and gas temperatures and radio priors on the sources, using MCMC to estimate key cluster parameters in the context of a β–model for the gas distribution. In this context, the CMB primordial fluctuations are an additional

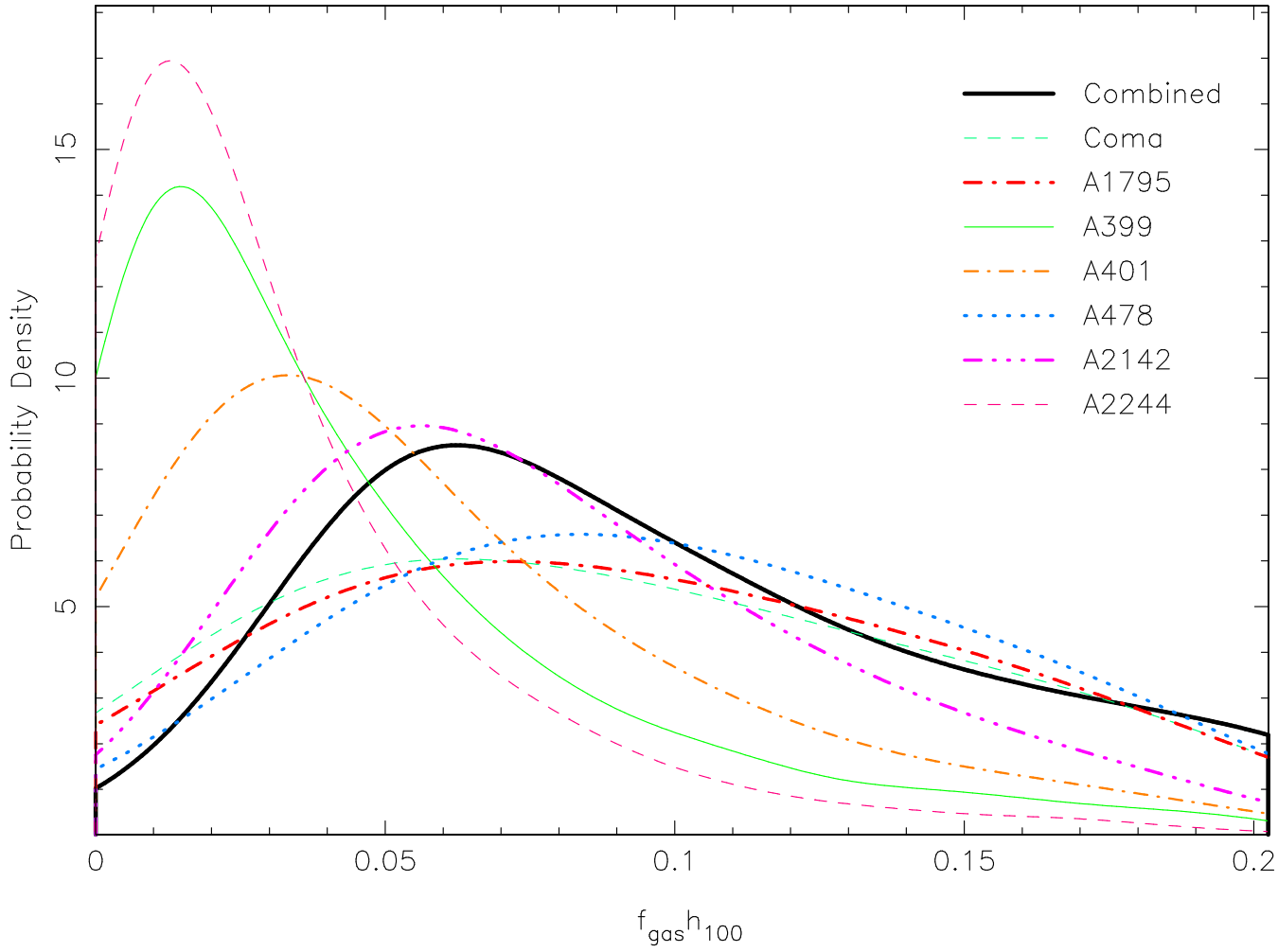

Figure 5. Plot of the probability distributions for $f_{\rm gas}$ for each cluster, and that derived from combining the full sample.

source of Gaussian noise, and are included in the model as a non–diagonal covariance matrix derived from the known angular power spectrum. We use the SZ data (plus the priors) to give both the gas mass and, under the assumption of hydrostatic equilibrium, the total mass. Although the data have high random errors, the use of Bayesian methods, probability density functions and marginalisation prevents bias in the results.

(iii) The degeneracy is evident between β and core radius as expected for such observations sensitive to SZ over a narrow ℓ–range. There are significant measurements of gas fractions in the detected clusters.

(iv) We present a normalisation of the M-T relation derived from our data which we find to be in good agreement with recent X-ray cluster measurements.

(v) Using the gas fraction probability density function for each cluster, we have produced combined gas fractions for the four detections, for the three non-detections, and for all seven. The Bayesian evidence shows that the first is the correct one to use in the context of trying to measure a low-z global gas fraction. For this we here find $f_{\rm gas} = 0.08^{+0.06}_{-0.04} h_{100}^{-1}$.

(vi) Gas fraction measurement by this SZ–based method is relatively immune from the effect of primordial CMB anisotropy. This is true since the effect on gas mass tends to cancel the effect on total mass on the narrow range of angular scale employed. Simulations show the cancellation to be good for contaminant fluxes of ± 50 mJy.

That the analysis method works as well as it does points the way towards analysis of data from upcoming SZ telescopes.

6 ACKNOWLEDGEMENTS

The authors thank the referee for useful comments and suggestions. We thank the staff of Jodrell Bank Observatory, the Mullard Radio Astronomy Observatory and the Teide Observatory for assistance in the day-to-day operation of the VSA. We thank PPARC and the IAC for funding and supporting the VSA project. Partial financial support was provided by the Spanish Ministry of Science and Technology, project AYA2001-1657. We thank Angela Taylor for processing and analysing the source subtractor observations for Coma. We also thank Clive Dickinson, Will Grainger, Charlie McLachlan and Jonathan Zwart for useful discussions. RK thanks Monique Arnaud and Sarah Church for interest-

ing conversations. KL acknowledges support of a PPARC studentship.

REFERENCES

Allen S., Schmidt R., A.C. F., 2002, MNRAS, 334, L11

Allen S. W., Schmidt R. W., Fabian A. C., 2001, MNRAS, 328, L37

Allen S. W., Schmidt R. W., Fabian A. C., Ebeling H., 2003, MNRAS, 342, 287

Arnaud M., Pratt G. W., Pointecouteau E., 2004, Memorie della Societa Astronomica Italiana, 75, 529

Böhringer H., Voges W., Huchra J. P., McLean B., Giacconi R., Rosati P., Burg R., Mader J., Schuecker P., Simiç D., Komossa S., Reiprich T. H., Retzlaff J., Trümper J., 2000, ApJS, 129, 435

Birkinshaw M., 1999, Phys.Rep., 310, 97

Bonamente M., Joy M. K., Carlstrom J. E., Reese E. D., LaRoque S. J., 2004, Markov Chain Monte Carlo joint analysis of Chandra X-ray imaging spectroscopy and Sunyaev-Zeldovich Effect data, preprint, `astro-ph/0403016`

Carlstrom J. E., Holder G. P., Reese E. D., 2002, ARA&A, 40, 643

Cavaliere A., Fusco-Femiano R., 1976, A&A, 49, 137

Cavaliere A., Fusco-Femiano R., 1978, A&A, 70, 677

Condon J. J., Cotton W. D., Greisen E. W., Yin Q. F., Perley R. A., Taylor G. B., Broderick J. J., 1998, AJ, 115, 1693

Cowles M. K., Carlin B. P., 1996, Journal of the American Statistical Association, 91, 883

Dickinson C., et al., 2004, High sensitivity measurements of the CMB power spectrum with the extended Very Small Array, preprint, `astro-ph/0402498`

Ettori S., Fabian A. C., 1999, MNRAS, 305, 834

Evrard A. E., 1997, MNRAS, 292, 289

Evrard A. E., Metzler C. A., Navarro J. F., 1996, ApJ, 469, 494

Finoguenov A., Reiprich T. H., Böhringer H., 2001, A&A, 368, 749

Gilks W. R., Richardson S., Spiegelhalter D. J., 1996, Markov-Chain Monte-Carlo In Practice. Cambridge: Chapman and Hall

Grainge K., et al., 2003, MNRAS, 341, L23

Grego L., Carlstrom J. E., Reese E. D., Holder G. P., Holzapfel W. L., Joy M. K., Mohr J. J., Patel S., 2001, ApJ, 552, 2

Gregory P. C., Scott W. K., Douglas K., Condon J. J., 1996, ApJS, 103, 427

Herbig T., Lawrence C. R., Readhead A. C. S., Gulkis S., 1995, ApJ, 449, L5+

Hobson M. P., Bridle S. L., Lahav O., 2002, MNRAS, 335, 377

Hughes J. P., Gorenstein P., Fabricant D., 1988, ApJ, 329, 82

King I., 1962, AJ, 67, 471

Kneissl R., Jones M. E., Saunders R., Eke V. R., Lasenby A. N., Grainge K., Cotter G., 2001, MNRAS, 328, 783

Lo K. Y., 2002, in ASP Conf. Ser. 257: AMiBA 2001: High-Z Clusters, Missing Baryons, and CMB Polarization The Current State of Astronomy in Taiwan and AMiBA. pp 3–+

Markevitch M., Forman W. R., Sarazin C. L., Vikhlinin A., 1998, ApJ, 503, 77

Marshall P. J., Hobson M. P., Slosar A., 2003, MNRAS, 346, 489

Mason B. S., Leitch E. M., Myers S. T., Cartwright J. K., Readhead A. C. S., 1999, AJ, 118, 2908

Mason B. S., Myers S. T., 2000, ApJ, 540, 614

Mason B. S., Myers S. T., Readhead A. C. S., 2001, ApJ, 555, L11

Mohr J. J., Carlstrom J. E., The SZA Collaboration 2002, in ASP Conf. Ser. 257: AMiBA 2001: High-Z Clusters, Missing Baryons, and CMB Polarization The SZ-Array: Configuration and Science Prospects. p. 43

Mohr J. J., Mathiesen B., Evrard A. E., 1999, ApJ, 517, 627

Myers S. T., Baker J. E., Readhead A. C. S., Leitch E. M., Herbig T., 1997, ApJ, 485, 1

Ó Ruanaidh J., Fitzgerald W., 1996, Numerical Bayesian Methods Applied to Signal Processing. New York: Springer-Verlag

Peacock J., 1999, Cosmological Physics. Cambridge: CUP

Pointecouteau E., Arnaud M., Kaastra J., de Plaa J., 2004, Markov Chain Monte Carlo joint analysis of Chandra X-ray imaging spectroscopy and Sunyaev-Zeldovich Effect data, preprint, `astro-ph/0403016`

Pratt G. W., Arnaud M., 2002, A&A, 394, 375

Rebolo R., et al., 2004, Cosmological parameter estimation using Very Small Array data out to l=1500, preprint, `astro-ph/0402466`

Reese E. D., Carlstrom J. E., Joy M., Mohr J. J., Grego L., Holzapfel W. L., 2002, ApJ, 581, 53

Rubiño-Martin J. A., et al., 2003, MNRAS, 341, 1084

Sanderson A. J. R., Ponman T. J., 2003, MNRAS, 345, 1241

Scheuer P. A. G., 1957, Proc. Cam. Phil. Soc., 53, 764

Scott P. F., et al., 2003, MNRAS, 341, 1076

Sivia D., 1996, Data Analysis: A Bayesian Tutorial. Oxford: OUP

Skilling J., 2002, BayeSys3 manual, unpublished, see http://www.maxent.co.uk

Slosar A., et al., 2003, MNRAS, 341, L29

Struble M. F., Rood H. J., 1991, ApJS, 77, 363

Sun M., Jones C., Murray S. S., Allen S. W., Fabian A. C., Edge A. C., 2003, ApJ, 587, 619

Sunyaev R. A., Zel'dovich Y. B., 1972, Comments on Astrophysics, 4, 173

Taylor A. C., et al., 2003, MNRAS, 341, 1066

Waldram E. M., Pooley G. G., Grainge K. J. B., Jones M. E., Saunders R. D. E., Scott P. F., Taylor A. C., 2003, MNRAS, 342, 915

Watson R. A., et al., 2003, MNRAS, 341, 1057

White S., Navarro J., Evrard A., Frenk C., 1993, Nature, 366, 429

Zhang Y.-Y., Finoguenov A., Böhringer H., Ikebe Y., Matsushita K., Schuecker P., 2004, A&A, 413, 49

This paper has been typeset from a TEX/ LATEX file prepared by the author.